17 (2023) 100278

Contents lists available at ScienceDirect

International Journal of Thermofluids

journal homepage: www.sciencedirect.com/journal/international-journal-of-thermofluids

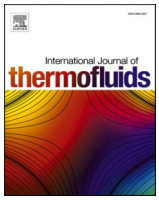

Heat transfer delay method for the fluid velocity evaluation in a multi-turn pulsating heat pipe

L Pagliarini [a], L Cattani [a], M Mameli [b], S Filippeschi [b,*], F Bozzoli [a]

[a] Department of Engineering and Architecture, University of Parma, Parco Area delle Scienze 181/A, Parma, Italy
[b] Department of Energy, Systems Land and Construction Engineering, University of Pisa, Largo L. Lazzarino, Pisa, Italy

ARTICLE INFO

Keywords:
Pulsating heat pipes
Local thermal analysis
Inverse heat conduction problem
Heat transfer delay method

ABSTRACT

A multi-turn closed loop pulsating heat pipe made of aluminium is tested in vertical bottom heated mode and different condenser temperatures with the aim of providing quantitative information regarding its flow dynamics through a novel post-processing technique on the local wall-to-fluid heat flux, evaluated within the adiabatic section. The studied device is made of an annealed aluminium tube (inner/outer diameter: 3/5 mm), folded in 14 turns and partially filled with methanol (volumetric filling ratio: 50%). The aluminium channels are coated with a high-emissivity opaque paint, thus allowing thermographic measurements on the outer wall by means of a high-resolution medium wave infrared camera. The proposed method, named Heat Transfer Delay Method, is validated by means of a dedicated experimental approach. Then, the acquired time-space temperature maps are used as input data for the inverse heat conduction problem resolution approach to estimate the local convective heat flux locally exchanged at the inner wall-fluid interface. The resulting wall-to-fluid heat fluxes are then post-processed by applying the Heat Transfer Delay Method to the oscillatory and circulatory flow modes. The average fluid velocity is assessed at varying working conditions during the circulatory flow, finding values up to 0.77 m/s and 0.3 m/s for condenser temperature equal to 20 °C and 10 °C, respectively.

1. Introduction

The electrical energy demand for the cooling of electronic systems is more and more increasing due to the continuous miniaturization process of electronic components, resulting in higher power densities to be dissipated [1,2]. Two-phase passive devices, such as Heat Pipes (HPs) and Pulsating Heat Pipes (PHPs), represent a suitable solution for this challenging thermal management issue [3,4]. Specifically, PHPs are achieving resounding interest within the scientific community due to their low manufacturing cost, good surface adaptability and high flexibility [5]. These fascinating features have been proven to be extremely useful in several thermal management applications, spanning from the automotive industry to the micro-electronics field [6,7], even though a large-scale employment of PHPs is nowadays undermined by a lack of knowledge concerning their working behaviour. This inevitably prevents the design of models able to reliably predict the PHP thermal performances. In fact, PHPs governing thermo-fluid dynamic principles are still not fully understood; since the PHPs thermal performance is influenced by the thermally induced motion of the working fluid, a detailed analysis on the flow dynamics is needed to achieve a complete description of the thermofluidic interactions occurring in such heat transfer devices.

Specifically, the flow dynamics in PHPs is usually described in terms of flow pattern, i.e., slug-plug, semi-annular or annular flow, flow mode, i.e., fluid oscillation or circulation, oscillation frequency and fluid velocity [8]. In particular, the flow pattern reflects the heat and mass transfer mechanisms inside the two-phase device at different operating conditions, while different flow modes may lead to different thermal performances. High thermal performances can be generally achieved with net fluid circulation, especially when coupled with annular flows [9,10]. On the other hand, the working fluid oscillation frequency is an important parameter that quantifies the heat transfer rate from the evaporator to the condenser, and, consequently, the heat transfer capability of the device [11]. Lastly, the evaluation of fluid velocity is crucial for understanding the flow patterns and the operational limits of PHPs in terms of inertial forces and flow transitions, i.e., liquid-vapour interfaces break-up [12].

From an experimental standpoint, the fluid velocity is usually estimated by means of direct fluid visualizations, achieved with transparent inserts/PHPs entirely made of transparent materials; few cases of direct measurements of the fluid pressure are also reported. Tong et al. [13]

* Corresponding author.
E-mail address: sauro.filippeschi@unipi.it (S. Filippeschi).

https://doi.org/10.1016/j.ijft.2022.100278

Available online 30 December 2022

Nomenclature

Symbol-Quantity-SI Unit

b, m	Correlation parameters -
c_p	Specific heat at constant pressure J/kg·K
f, g	Signals, functions of time -
H	Gaussian filter transfer function -
i	Channel number -
k	Thermal conductivity W/m·K
L	Length m
M	Number of time samples -
N	Number of axial coordinates -
n	Number of channels K/W
q	Convective heat flux per unit surface W/m^2
Q	Power input provided to the evaporator W
r	Tube radius m
R^2	Coefficient of determination -
r^*	Normalized cross-correlation function -
R_{env}	Overall heat-transfer resistance between the external tube wall and the surrounding environment m^2·K/W
S	Cross-sectional area of the channel m^2
t	Time s
T	Temperature K, °C
u, v	Frequency components rad^{-1}
u_c	Cut-off frequency rad^{-1}
v	Fluid velocity m/s
V	Volume m^3
v_{av}	Average fluid velocity m/s
v_m	Measured fluid velocity through flow rate calculation m/s
z	Axial coordinate m
δ	Uncertainty -
ρ	Density kg/m^3
σ	Noise level K, °C
τ	Time lag s

were amongst the first researchers to provide a description of the oscillatory/circulatory operation in a glass PHP filled with methanol in terms of fluid dynamics. In particular, once a net fluid circulation was attained in vertical orientation, an increase of fluid velocity with the power input to the evaporator was assessed by means of a charge-coupled device for high-speed visualization, even though no quantitative data were provided. Also, the circulatory flow presented local oscillations of the slugs. Xu et al. [14] investigated through visible light imagining (sampling frequency = 125 Hz) a 4-turn PHP entirely made of glass. The evaporator, thermally insulated to minimise heat losses, was warmed up by a heating coil, while heat dissipation at the condenser (directly exposed to the external environment) was achieved by free convection with air and radiation. The device was charged with two working fluids, namely methanol and deionized water; the filling ratio was equal to 70% for both fluids. The study revealed interesting remarks regarding the fluid stream, such as presence of bulk circulation, bubble coalescence/break-up at the condenser, different flow patterns at varying heat loads and liquid-vapour distribution. The quasi-sine oscillation of both displacement and velocity of methanol during the PHP operation was also reported; the deionized water exhibited instead a quasi-rectangular bubble displacement. In [14], the velocity was evaluated by differentiating the bubble displacement against time, with uncertainty ranging from 0.1% up to 10% for velocities of 100 mm/s and 1 mm/s, respectively. The mean velocity for water during the so-called "fast movement" period was assessed equal to 180 mm/s at 30 W to the evaporator. Xue and Qu [10] performed visualization experiments on a glass PHP charged with ammonia. Contrarily to [14], no thermal insulation was applied to the evaporator due to visualization purposes, and dissipations at the condenser were obtained by forced convection with cooling water. Nonetheless, the fluid velocity was estimated through the same approach. By considering the accuracies of measured displacement and travelling times equal to ± 0.5 mm and ± 1/15 ms, respectively, the uncertainty of the evaluated velocities was assessed through propagation of errors. The instantaneous fluid velocities were reported in the ranges 0.1–0.6 m/s and 0.4–0.9 m/s for the slug-plug flow and the annular flow, respectively. An analytical model for the prediction of the thermofluidic behaviour was furtherly proposed in [10], showing a good agreement between theoretical and experimental results in terms of velocity and flow pattern. However, such a prediction model may not be extended to other experiments adopting different wall materials or boundary conditions at the two heat transfer sections, such as thermally insulated evaporator and/or free convection with air at the condenser. Pietrasanta et al. [15] conducted experimental visualizations and dimensionless investigations on the evolution of the flow pattern in a single loop PHP having a sapphire insert with ethanol and FC-72 as working fluids. The device was tested in standard, micro and hyper-gravity. The fluid velocity was measured through a Particle Image Velocimetry (PIV)-based method with sampling frequency of 100 Hz. The menisci were tracked by detecting differences in pixel intensity in the acquired images. The PIV software, calibrated through synthetic frame series, allocated velocity values for each node in the considered grid, with a maximum estimation error of 0.0066 m/s. For ethanol, interface velocities exhibited a maximum of about 0.4 m/s in both standard and hyper-gravity, whereas the latter condition ensured generally higher fluid accelerations. During microgravity, the ethanol-charged device did not operate, while the FC-72 velocity showed peaks of 0.1–0.2 m/s. Additionally, in [15], a flow pattern transition map between slug-plug and annular flows was defined by a fluid velocity and acceleration analysis based on the employment of modified Bond, Froude and Weber numbers. Patel and Mehta [16] provided a complete channel wise displacement-velocity-frequency analysis on the fluid flow in a PHP charged with acetone (filling ratio: 50%) by means of visualization experiments. The layout was made of a copper capillary tube, whereas glass inserts were placed within the adiabatic section. The acquisitions were processed through the Photron FASTCAM Analysis software, and specified targets were tracked in terms of displacement, velocity and acceleration of the working fluid. During the experiments, transitions between slug-plug and unidirectional flows with overlaid oscillations were observed. Such a unidirectional flow exhibited differences in terms of mean velocity from upwards to downwards channels. In the former branches, the fluid velocity increased from 0.230 m/s up to 0.565 m/s at 50 W and 100 W, respectively, while in the latter, it increased from 0.142 m/s up to 0.272 m/s. In [16], the velocity averagely assumed by the working fluid in the whole device from 10 to 100 W was furtherly shown. The average fluid velocity values ranged in between 0.01 m/s (10 W) and 0.42 m/s (100 W), and their trend was found to follow a power law of the form $Y = 0.0004\ X^{1.5147}$ (Y: fluid velocity; X: heat load to the evaporator; $R^2 = 0.9958$). Heat loads higher than 100 W could not be similarly investigated in terms of average fluid velocity since the adopted bubble tracking technique was undermined by the presence of deformed menisci, especially in the upwards channels. Perna et al. [17] proposed a novel method for the evaluation of the average fluid velocity in a 14-turn PHP under microgravity conditions by estimating the phase shift between the fluid pressure signals acquired near the evaporator and the condenser in one single branch. The relationship between fluid pressure variations in a single branch and fluid motion in PHPs was previously demonstrated in [18]. The pressure acquisitions were first processed through the wavelet method to assess fluid dominant oscillation frequencies. The distance between the two fluid pressure measurement

points at the evaporator and condenser sections was therefore divided by the time lag between the two acquired pressure signals. The found values fell in the range 0.09–0.13 m/s. Abela et al. [19] conducted a multi-parametric transient numerical study on the same PHP of [17] to assess the agreement with experimental data collected during a parabolic flight campaign within the start-up phase. Experimental initial and boundary conditions were given to the model, i.e., by starting before the delivery of input power to the system. The results showed a good agreement between numerical outputs and experimental remarks: wall temperature evolutions over transient and pseudo-steady state periods were captured within 7%, while pressure signals agreed only qualitatively with the model. Direct infrared visualization of the working fluid (sampling rate = 50 Hz) through a sapphire insert additionally allowed liquid temperature measurements, along with the evaluation of vapour/liquid displacement and liquid plugs velocity by means of the menisci tracking technique described in [17]. In particular, the velocity peaks estimated in [19] fell in the range 0.03–0.1 m/s, during microgravity conditions and for low and high heat loads to the evaporator, respectively. For the reported cases, simulations were able to satisfactorily predict the fluid velocity in terms of general trends and peak values.

However, transparent inserts or pressure transducers directly

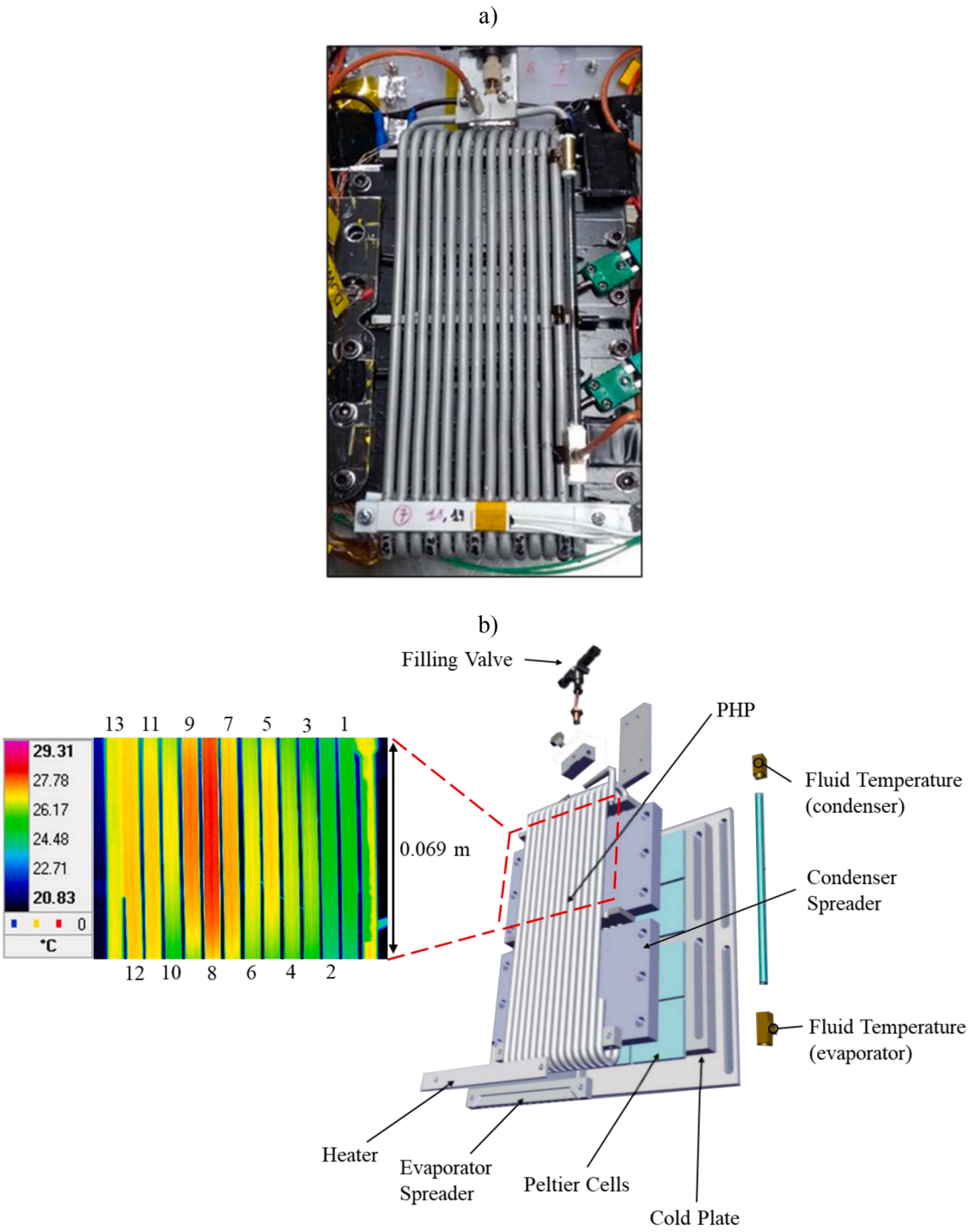

Fig. 1. Test rig (a) and exploded view of the studied PHP, experimental equipment location and sample of raw IR measurement (b), with reference to the 13 aluminium channels numeration.

inserted in the fluid flow highly increase the cost and complexity of experimental set-ups especially for what concerns tubular PHPs, thus leading to high manufacturing efforts or perturbations of the inner flow. In addition, common flow visualization techniques for the fluid velocity evaluation necessarily rely on the presence of stable and recognizable fluid menisci, which could not be always obtained for every test condition. The complexity of post-processing methods involving tracking procedures should be furtherly taken into account.

Hence, the present work proposes to quantify the average fluid velocity in PHPs without adopting any of the previously mentioned techniques, which could be significantly intrusive for the device operation. To this aim, InfraRed (IR) acquisitions, carried out on the outer surface of a 14-turn CLPHP already characterized at different orientations [20], are used as input parameters for the Inverse Heat Conduction Problem (IHCP) resolution approach. It has to be stressed that such an inverse approach has been already adopted to quantitatively describe the thermofluidic behaviour of tubular and micro-PHPs in terms of statistical coefficients and fluid oscillation frequencies [20–22]. Nonetheless, when compared to the previous literature, the present experimental investigation furtherly applies a novel data reduction technique on the resulting heat fluxes exchanged between the working fluid and the device wall, named Heat Transfer Delay Method (HTDM). Such a method, validated by means of an experimental approach, is based on normalized cross-correlation functions between adjacent channels to evaluate the time taken by the working fluid to travel through the entire device. The average fluid velocity is consequently assessed at varying heat loads to the evaporator and condenser temperatures during the circulatory flow operation. To the Authors' knowledge, this represents the first attempt of estimating average fluid velocities in PHPs through cross-correlations of local wall-to-fluid heat fluxes. The proposed method can be applied to the experimental study of any metallic PHPs, even when their experimental apparatus has not been explicitly designed for the fluid velocity evaluation. In other words, the proposed technique is not only intended to enrich the literature database with original outcomes, but it also and mainly aims at providing a useful tool that allows to infer on the fluid velocity inside a thermofluidic device without the need for visualization inserts nor other intrusive fluid measurements, making the analysis more independent from the observer.

2. Experimental set-up

The studied device (Fig. 1), specifically designed to fit the limiting constraints of the Heat Transfer Host aboard the International Space Station [23], is made of an annealed aluminium tube (6060 alloy, inner/outer diameter = 3/5 mm), shaped in a 3-D closed loop layout (overall size: 220 × 80 × 25 mm, 14 turns). One of the aluminium channels is replaced with a sapphire insert for flow visualization. Two aluminium heat spreaders (100 × 12 × 10 mm) are brazed on the tube in the evaporator zone, holding two ceramic ohmic heaters (Innovacera®, electrical resistance 18 Ω ± 10). The evaporator section is insulated by means of a layer (0.01 m) of insulating material. The heating power is provided by a programmable power supply (GW-Instek®, PSH-6006A). The condenser zone is embedded between two aluminium heat spreaders (80 × 120 × 10 mm), cooled by means of a Peltier cell system (eight Peltier cells by Adaptive Thermal Management®, ETH-127–14–11-S; control system by Meertstetter Engineering®, TEC 1123) coupled with a cold plate temperature control system loop (Aavid Thermalloy®).

The fluid temperature measurement was performed by two K-type micro-thermocouples (Omega® KMTSS-IM025E-150, bead diameter 0.25 mm, response time 0.1 s with 95% confidence, 10 Hz) inserted in the fluid flow. The 13 aluminium channels within the adiabatic section, numbered in Fig. 1, were uniformly coated with a high-emissivity opaque paint (ε = 0.92), and the outer wall temperature was acquired by a high-resolution Medium Wave InfraRed (MWIR) camera (FLIR® SC7600, 18 Hz, 640 × 512 pixels) over a 6.9 cm high portion, highlighted in red in Fig. 1b.

The device was first evacuated (down to 10^{-6} mbar) and then partially filled by means of a micro-metering valve (IDEX® Upchurch *Sc*. P-447) with methanol (filling ratio = 50 ± 1% vol.). In particular, methanol was chosen amongst other fluids since, according to the static Bond criterion [3], it guarantees a capillary flow inside the considered device in standard gravity condition. Such a specific selection was additionally driven by the low viscosity of the working fluid, especially for the sake of previous investigations on different tilt angles [20], coupled with a low saturation pressure, which is highly needed for junctions' integrity and leaks prevention at average/high heat loads.

During the experiments, the device was tested in vertical bottom heated mode. The condenser temperature was set to 10 °C and 20 °C, while the heat load to the evaporator was varied from 10 W up to 210 W. IR acquisitions (60 s each) were carried out within the pseudo-steady states of the system, i.e., after about 25 min from each power input step to the evaporator. The IR camera parameters and settings employed during the experiments are listed in Table 1.

For safety reasons, the evaporator temperature was limited to a maximum of 105 °C by a thermal switch, directly placed on the evaporator heater. Hence, the thermal switch activation was avoided by setting, case by case, different upper limits to the providable power input to the evaporator.

3. Methods

3.1. Heat flux evaluation

The local convective heat flux q exchanged at the inner fluid-wall interface, was evaluated starting from the temperature distribution on the channels outer surface acquired by the IR camera within the adiabatic section.

As already pointed out by Pagliarini et al. [22], the test section, outlined in Fig. 2, can be modelled as an axisymmetric 1D domain by considering negligible the temperature gradient along the circumference and by assuming the outer surface temperature equal to the one at the inner surface (thin wall approximation).

Starting from the local energy balance equation at the infinitesimal wall section, the heat flux on the wall inner surface can be obtained from the following equation, thoroughly explained in [22]:

$$q = \frac{\left(\rho c_p \frac{\partial T}{\partial t} - k \frac{\partial^2 T}{\partial z^2}\right)\left(r_{ext}^2 - r_{int}^2\right) + \frac{(T - T_{env})}{R_{env}} 2 r_{ext}}{2 r_{int}} \quad (1)$$

where k is the thermal conductivity of the aluminium channel (≈ 201 W/mK at 300 K), T_{env} is the environmental temperature and R_{env} is the overall heat-transfer resistance between the channel wall and the surrounding environment, assumed equal to 0.1 m^2K/W, which is a representative value for air natural convection with radiative heat transfer towards the environment [24].

Being the measured wall temperature unavoidably noisy, Eq. (1) gives unstable results especially due to the presence of the second-order derivative [25]. Such an issue can be successfully faced by filtering out the high-frequency, noisy components from the raw temperature data

Table 1
IR camera parameters and settings.

Wavelength	1.5 - 5.1 μm
Focal length	25 mm
F-number	3
Cooler	Close-cycle (rotary) stirling cooler
Field of view	22° x 17°
Temperature range	5 °C to 300 °C
Absolute uncertainty	1 °C
Sensitivity	< 25mK
Distance from the framed portion during the tests	40 cm

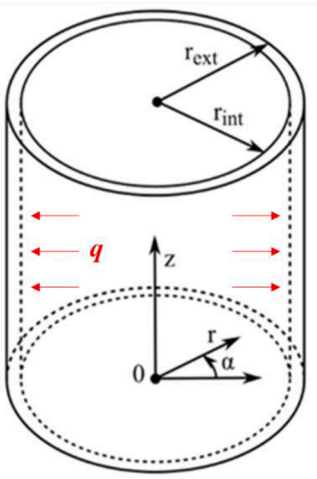

Fig. 2. Sketch of the test section.

[26–28]. By adopting the reasonable assumption that the noise level presents a Gaussian distribution, a Gaussian filter is here employed. According to its bidimensional formulation, the transfer function of the Gaussian filter along the two dimensions u and v (representative of t and z) is defined in Eq. (2).

$$H(u,v) = e^{-\left(u^2+v^2\right)/2u_c^2} \tag{2}$$

Since in real applications the optimal cut-off frequency u_c value is not known a priori, in the present analysis the criterion provided by the discrepancy principle, originally formulated by Morozov [29], was adopted. According to this principle, the problem solution is regarded to be sufficiently accurate when the difference between the measured T and filtered T_f temperatures is close to the standard deviation of the raw measurements:

$$\frac{T_f - T_2}{\sqrt{N \cdot M}} \cong \sigma \tag{3}$$

where $||\ ||_2$ stands for the 2-norm, N and M are the sizes of the T matrix (N axial coordinates, M time samples) and σ is the standard deviation of the raw data, estimated by measuring the wall temperature distribution while maintaining the system under isothermal conditions. σ was found to vary from 0.04 K at high temperature, i.e., for PHP configurations at $T_{cond} = 20$ °C, to 0.06 K at low temperature, i.e., for PHP configurations at $T_{cond} = 10$ °C, due to the specifications of the adopted IR camera.

By adopting the filtered temperature T_f, Eq. (1) can be finally solved by means of the finite difference method. The estimation error for the present approach applied to the here considered device ranged from about 9% to a maximum of 21%. For further information regarding the validation of the local heat flux estimation procedure, see [22].

3.2. Heat transfer delay method

The estimated local wall-to-fluid heat fluxes were reduced through the HTDM, which is based on normalized cross-correlation functions between local thermal interactions in adjacent channels of the studied PHP. In particular, the cross-correlation r_{fg} between two finite discrete functions of time f and g and length M is defined in Eq. (4) [30].

$$r_{fg}(\tau) = \sum_{t=0}^{M} f(t)g(t+\tau) \tag{4}$$

To obtain an accurate and comparable estimation of the cross-correlation, the normalized cross-correlation function r^*_{fg} is usually adopted in place of r_{fg}:

$$r^*_{fg}(\tau) = \frac{1}{\sqrt{r_{ff}(0)r_{gg}(0)}} r_{fg}(\tau) \tag{5}$$

where τ is the displacement (or lag) between f and g, $r_{ff}(0)$ and $r_{gg}(0)$ are the autocorrelations of f and g at zero lag, respectively, and r_{fg} is the cross-correlation between the two functions.

The cross-correlation essentially shifts the function g along the time axis, calculating, for each single time shift τ, the sum of the product between f and g. Hence, when a proper overlap of the two functions is reached, r_{fg} and, consequently, r^*_{fg} are maximized and the time lag τ_0 between the original signals can be assessed. Other low-amplitude peaks of r^*_{fg} depend on the shape of the given functions, and they are not to be considered as representative of the actual time delay. However, the evaluation of τ cannot be achieved when a correlation between the two signals is not present, i.e., when $r^*_{fg}(\tau_0)$ assumes significantly low values. The maximum peak of r^*_{fg} can be noted either at positive or negative time lags: specifically, when $\tau > 0$, g is in advance with respect to f. Moreover, values of the r^*_{fg} peaks greater than 0.6 are usually adopted as representative threshold for the assessment of a meaningful cross-correlation between the analysed signals, while lower values denote instead poor correlation.

It has to be highlighted that the time shift in Eq. (4) depends on the particular discretization of the two input functions. Hence, the time lag at which r_{fg} is maximized is intrinsically affected by an error equal to ± 1 time shift. While, for densely discretized functions, the time shift is low (i.e., low estimation error for the time lag), for poorly discretized functions, the time shift becomes higher (i.e., high estimation error for the time lag). The goodness of the estimated time lag thus depends on the time discretization specifically adopted for f and g.

When, in a given physical system, the two analysed signals referred to two spatial points a and b at a distance $L_{[a \to b]}$ are due to a common perturbating phenomenon, e.g., pressure variations caused by sound waves or temperature variations caused by moving heat sources, the evaluated time lag $\tau_{[a \to b]}$ is related to the travel time of the accounted perturbation. Hence, the velocity $v_{[a \to b]}$ of the perturbating phenomenon can be evaluated as follows:

$$v_{[a \to b]} = \frac{L_{[a \to b]}}{\tau_{[a \to b]}} \tag{6}$$

The uncertainty $\delta v_{[a \to b]}$ related to the velocity estimation of Eq. (6) is evaluated by means of the following definition [31]:

$$\delta v_{[a \to b]} = \sqrt{\left(\frac{\partial v_{[a \to b]}}{\partial L_{[a \to b]}} \delta L_{[a \to b]}\right)^2 + \left(\frac{\partial v_{[a \to b]}}{\partial \tau_{[a \to b]}} \delta \tau_{[a \to b]}\right)^2} \tag{7}$$

where $\delta L_{[a \to b]}$ is the uncertainty referred to the travelled length and $\delta\tau_{[a \to b]}$ is the uncertainty of the time delay, defined as the reciprocal of the time step of the discretized functions f and g.

3.3. Heat transfer delay method validation

To validate the HTDM by means of an experimental approach, i.e., verifying that the thermal properties of the PHP wall allow an evaluation of fluid velocity by means of outer wall temperature measurements, a dedicated test rig is employed (Fig. 3). Specifically, it consists of a loop made up of a thermal bath (HAAKE® DC5 circulator) filled with pure water and an aluminium tube having the same inner/outer diameter and thermal properties of that used for the PHP manufacturing. Connections between the thermal bath and the aluminium channel are obtained by plastic tubes and LEGRIS® junctions. The aluminium tube is externally coated with the same highly emissive paint used for the set-up of Section 2 to monitor the outer wall temperature over a 0.23 m long tube portion by means of the same IR camera adopted for the PHP experimental analysis. The distance of the IR camera lens from the framed portion was

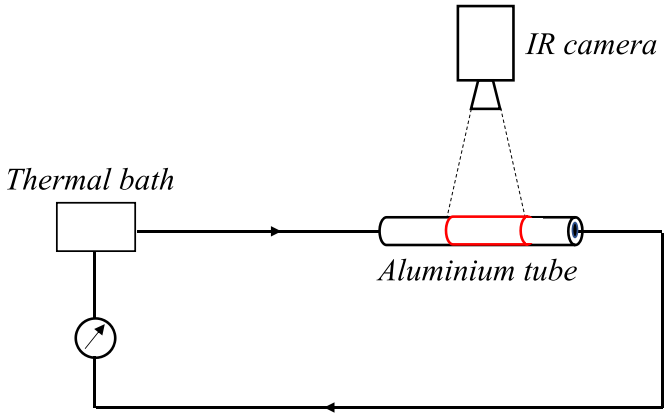

Fig. 3. Test rig for the HTDM validation.

the same as that reported in Table 1. Thermograms were sampled with same frequency of the tests described in Section 2 (18 Hz).

Before the test, the loop was at isothermal conditions with the environment, i.e., at 31 °C, and entirely filled with ambient air. The water temperature was therefore increased up to 70 °C by internally circulating the liquid inside the thermal bath. Once the set-point temperature was reached, the external circulation was switched on, thus letting the hot water flowing inside the loop. The volumetric flow rate guaranteed by the circulation pump is assessed by measuring the time required for filling a graduated cylinder at the thermal bath inlet, i.e., at the end of the loop. Such a measurement procedure was replicated 10 times to reduce errors introduced by the operator, thus having a significant number of data to be averaged. The fluid velocity was therefore assessed by dividing the measured flow rate by the tube inner diameter. Given the uncertainty of volume measurements $\delta V = 1$ ml, the uncertainty of time measurements $\delta t = 0.2$ s and the uncertainty related to the tube inner radius $\delta r = 0.1$ mm, the uncertainty of the measured velocity δv_m was assessed through propagation of errors [31] in Eq. (8). The uncertainty referred to the cross-sectional area S of the channel was estimated as $\delta S = 2S\delta r/r$.

$$\delta v_m = \sqrt{\left(\frac{\partial v_m}{\partial V}\delta V\right)^2 + \left(\frac{\partial v_m}{\partial t}\delta t\right)^2 + \left(\frac{\partial v_m}{\partial S}\delta S\right)^2} \tag{8}$$

The fluid velocity assessment was successfully reproduced during the pump operation to prove that the provided flow rate was constant over time.

Three different velocities were tested, namely 0.2, 0.4 and 1 m/s. The transient thermal interaction between the hot water and the aluminium tube, initially in thermal equilibrium with the environment, was caught, for every considered test condition, by means of thermography. In Fig. 4, the progressive increase of outer wall temperature due to inner convection is depicted by means of three IR acquisition samples ($t = 0$: start of the IR acquisition, before activating the circulation pump) for fluid velocity equal to 0.4 m/s (the fluid flows from left to right).

In Fig. 5, the space-time temperature map referred to the outer surface of the channel is shown to provide additional pieces of information on the temperature evolution with respect to those partially outlined in Fig. 4. Since the outer wall temperature was assumed as constant along the circumferential direction [22], only the maximum measured temperature (maximum emissivity), for each axial position, was selected as representative of the whole circumference. For this reason, the wall temperature samples were reduced to space-time maps, only dependant on the axial coordinate z and time. In particular, such a preliminary procedure on the acquired thermograms was carried out to avoid emissivity variations due to curvature effects and possible non-uniformities of the coating in the raw thermographic measurements.

The measured outer wall temperature is used as input for the IHCP resolution approach, thus evaluating the wall-to-fluid locally exchanged. Fig. 6a reports the wall temperature referred to the two fixed axial coordinates, namely $z = 0.015$ m and $z = 0.22$ m (reference of Fig. 4), while the corresponding evaluated wall-to-fluid heat fluxes are shown in Fig. 6b. Until about 6 s, the wall temperature is constant in both considered points (isothermal conditions, before water circulation in the loop). Hence, the wall-to-fluid heat flux is almost null within the same considered observation window. When hot water starts flowing inside the tube, the temperature trends undergo a sharp increase, resulting in high peaks in the evaluated heat fluxes.

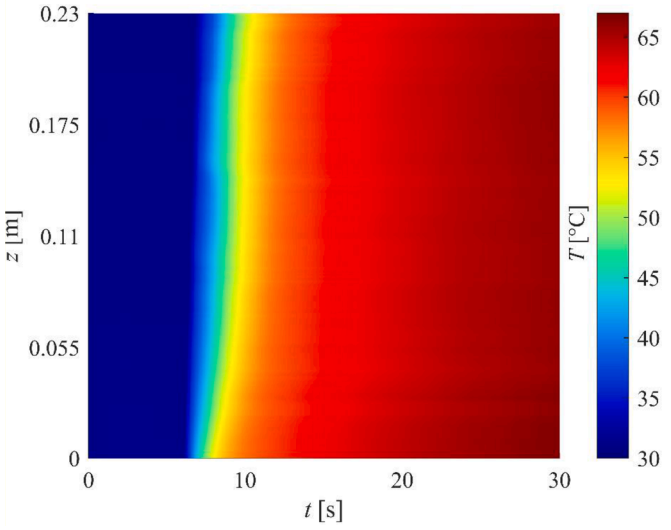

Fig. 5. Space-time evolution of outer wall temperature during the validation case of Fig. 4.

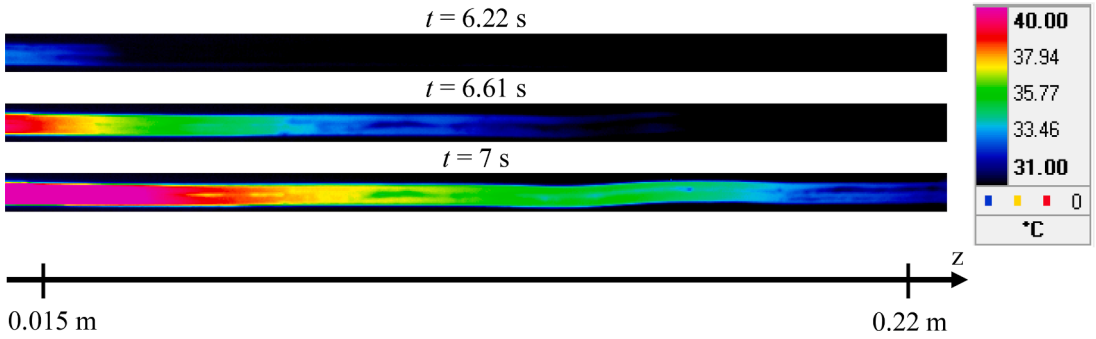

Fig. 4. Acquired thermographic samples of the transient thermal interaction between the hot fluid and aluminium tube at three different times t, for fluid velocity equal to 0.4 m/s.

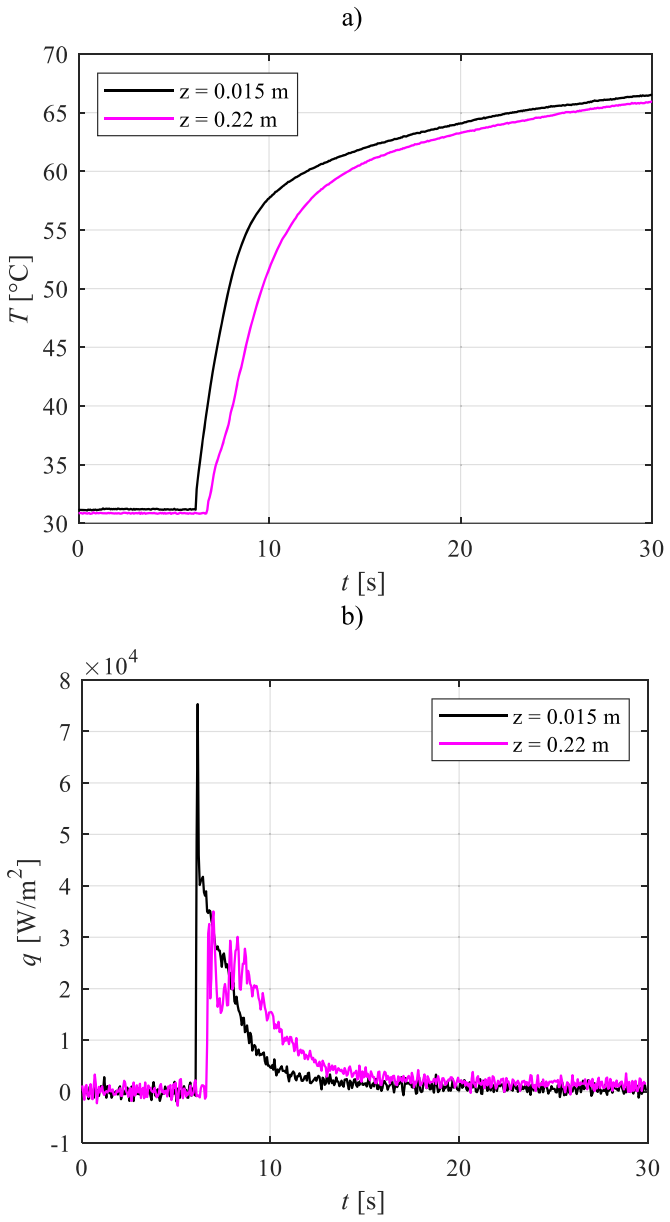

Fig. 6. Wall temperature acquired at two axial coordinates (a) and corresponding wall-to-fluid heat fluxes (b).

In addition, a certain time delay between the heat fluxes is clearly perceivable over the entire transient, suggesting that the thermal interactions occur in sequence; such a behaviour is noticeable for every considered fluid velocity. To quantify the time delay between the thermal interactions occurring at the two points of interest, the heat fluxes are adopted in Eqs. (4) and (5) by using the heat flux referred to z = 0.015 m as f and the one referred to z = 0.22 m as g. The resulting normalized cross-correlation functions are shown in Fig. 7. Here, the peaks are all at negative lags. According to its formulation, negative lags in the cross-correlation mean that the function f is in advance with respect to g, thus confirming the given flow direction along the tube axis (Fig. 4).

The delays evaluated for each fluid velocity are reported in Table 2. As expected, the time between the two consecutive thermal interactions decreases with the increase of the fluid velocity.

The estimation error for τ, as discussed in Section 3.2, is here equal to the reciprocal of the IR camera sampling rate, i.e., 1/18 ≈ 0.06 s. By adopting the distance between the two axial coordinates L = 0.22–0.015 m and the estimated τ in Eqs. (4) and (5), the fluid velocities are finally evaluated by means of Eq. (6). For comparison, the velocities measured trough the flowrate calculation are listed in Table 3 along with the ones evaluated through the HTDM and the corresponding uncertainties.

Specifically, the reported uncertainties were estimated through Eqs. (8) and (7) for the measured and evaluated velocities, respectively. Due to a proper overlap of the uncertainty bands, a good agreement between the two quantities is verified over the whole range of considered velocities. It has to be pointed out that, at high fluid velocity (1 m/s), the HTDM data are affected by significant uncertainty. In fact, higher velocities result in lower time delays between the accounted perturbations (heat flux signals), with consequently higher percentage errors on the estimation of the time lag τ by means of cross-correlations ($\delta\tau$ = 0.06 s). It has to be pointed out that, even though the present validation case is not perfectly reflecting the two-phase, chaotic flow inside the studied PHP, thermal interactions between the working fluid and the aluminium walls have been proven to allow a reliable and consistent evaluation of the fluid velocity by means of techniques based on thermography. The method can be extended to any tubular PHP having conductive walls, without the need of designing a complex experimental apparatus with transparent inserts or pressure transducers.

4. Results

4.1. Wall-to-fluid heat fluxes

For every study case, the IR acquisitions on the adiabatic section were post-processed by means of the procedure presented in Section 3.1, resulting in time-space heat flux distributions referred to each of the 13 analysed channels.

The wall temperature distribution and the corresponding wall-to-fluid heat flux distribution are reported in Fig. 8a and Fig. 8b, respectively, for channel 3, Q = 90 W, T_{cond} = 10 °C. For clarification, the evaporator is located below the considered portion (z < 0 m), while the condenser stands above (z > 0.069 m). Moreover, according to the adopted reference system, the heat flux distribution assumes positive values when the heat flux is transferred from the fluid to the channel wall. Hence, positive heat fluxes may correspond to the passage of hot fluid from the evaporator to the condenser. On the other hand, negative heat fluxes may generally denote flow reversal phenomena, during which cold fluid flows from the condenser to the evaporator at a lower temperature than that of the channel wall, previously heated by hot fluid coming from the evaporator. Null heat fluxes denote instead local stopovers, i.e., absence of fluid motion through the considered branch.

From a previous analysis on the present device under same test conditions [20], the flow modes, namely the oscillatory and circulatory flow, were identified by adopting both the fluid pressure signals and the evaporator temperature fluctuations. In Table 4, the identified flow modes are reported at different PHP working conditions.

The fluid flow mode reflected on the wall-to-fluid heat flux distributions due to greatly different thermofluidic interactions at the inner wall-fluid interface. Such peculiar local heat transfer behaviours are depicted in Fig. 9 and Fig. 10 for the oscillatory and circulatory flow, respectively. In Fig. 9, the temperature distributions referred to channel 3 (Fig. 9a) and 4 (Fig. 9b) are reported together with the corresponding wall-to-fluid heat fluxes (Fig. 9b-d, respectively) for T_{cond} = 20 °C and Q = 70 W (oscillatory flow). Here, the wall temperature and wall-to-fluid heat flux oscillate regularly for most of the observation window in channel 3 (Fig. 9a-b), denoting fluid motion over time. In channel 4, the two quantities vary only at the end of the observation window (Fig. 9c-d), denoting instead an almost total absence of fluid motion. Hence, during the oscillatory flow, the thermal interactions significantly differ from channel to channel due to the different fluid dynamic behaviour experienced in each device branch.

On the other hand, during the circulatory flow, the thermofluidic interactions between the working fluid and the device wall result in

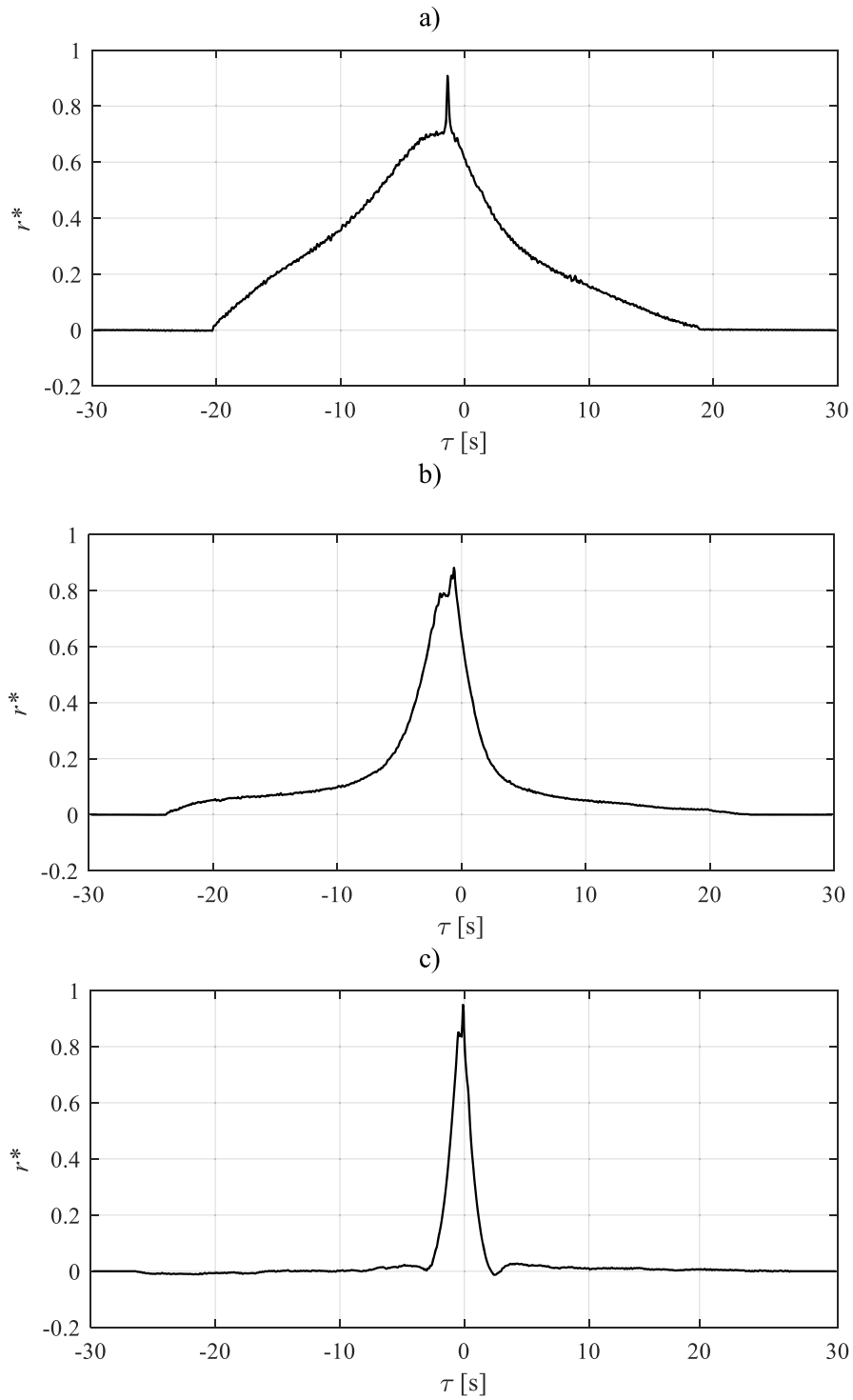

Fig. 7. Normalized cross-correlation functions, resulting from the post-processing of the heat fluxes referred to the two different axial coordinates for fluid velocity equal to 0.2 (a), 0.4 (b) and 1 m/s (c).

Table 2
Evaluated time lags for each considered fluid velocity.

Measured fluid velocity [m/s]	τ [s]
0.2	−1.39
0.4	-0.61
1	-0.22

Table 3
Comparison between measured and estimated fluid velocities.

Measured fluid velocity (flow rate calculation) [m/s]	Evaluated fluid velocity (HTDM) [m/s]
0.2 ± 0.03	0.15 ± 0.02
0.4 ± 0.05	0.34 ± 0.05
1.0 ± 0.1	0.9 ± 0.2

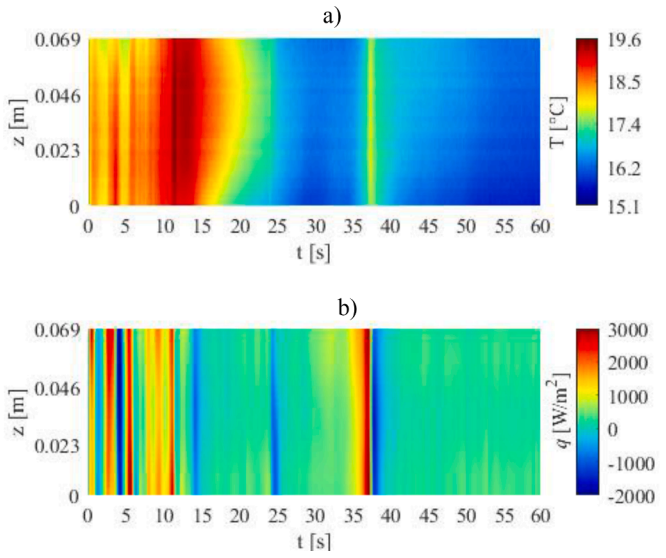

Fig. 8. Raw IR measurement (a) and corresponding wall-to-fluid heat flux distribution (b), referred to channel 3 at 90 W, T_{cond} = 10 °C.

Table 4
Flow modes identified in [20] for the same device at different working conditions.

Working condition		Identified flow mode
T_{cond} = 20 °C	Q < 90 W	Oscillatory flow
	$Q \geq$ 90 W	Circulatory flow
T_{cond} = 10 °C	Q < 120 W	Oscillatory flow
	$Q \geq$ 120 W	Circulatory flow

similar temperature (Fig. 10a-c) and heat flux (Fig. 10b-d) distributions, although shifted of few seconds. Such a shift results from the preferential flow direction assumed by the working fluid, which thermally interacts with the PHP wall in-series.

4.2. Heat transfer delay method: application to the oscillatory flow

A first application of the HTDM was attempted for the oscillatory flow cases reported in Table 4. Since fluid oscillations were found to differ from branch to branch Section 4.1), two axial positions belonging to the same channel (z = 0.01 m and z = 0.06 m) were here considered. Specifically, the two axial points were chosen near the edges of the observation window to maximize their relative distance. This selection is required to attempt an evaluation of instantaneous fluid velocity during the oscillatory flow, since lower distances result in a null time shift between the considered signals due to reasonably high velocities of the working fluid. It has to be stressed that the two coordinates z = 0 m and z = 0.069 m (borders of the heat flux map) were not here conservatively considered due to the well-known issue of edge degradation in the Gaussian filter [32]. The heat flux distributions referred to such locations were therefore used as inputs for Eqs. (4) and ((5), resulting in the evaluation of normalized cross-correlation between the two functions. In Fig. 11a, the used heat flux signals for Q = 70 W, T_{cond} = 10 °C (channel 11) are shown, while r^* is reported in Fig. 11b.

Here, the two considered heat fluxes (Fig. 11a) are perfectly in phase, suggesting that no variations in terms of spatial position can be perceived. This is proven by the peak in the cross-correlation (Fig. 11b) at τ = 0 s, i.e., the two curves are not delayed one with respect to the other. Such a behaviour is probably due to the coupled effect of great fluid velocity and low distance between the two considered points, which hampers a proper identification of the moving perturbation along the channel and, consequently, of the instantaneous fluid velocity by means of the HTDM. Such a remark was verified for every other test condition dominated by oscillatory flows. However, it has to be highlighted that, when impulsive phenomena occur, i.e., highly intermittent flow at low power inputs, a perceivable delay between the two heat fluxes is experienced. This is noticeable from Fig. 12, where the heat fluxes referred to the same axial coordinates of Fig. 11 for Q = 70 W, T_{cond} = 20 °C (channel 1) are shown along with the normalized cross-correlation between them. Specifically, the cross-correlation (Fig. 12b) exhibits a peak at τ = - 0.28 s, denoting also that the first heat flux profile (at z = 0.01 m) is in advance with respect to the second one (at z = 0.06 m), i.e., that the fluid flows from the evaporator to the condenser. The

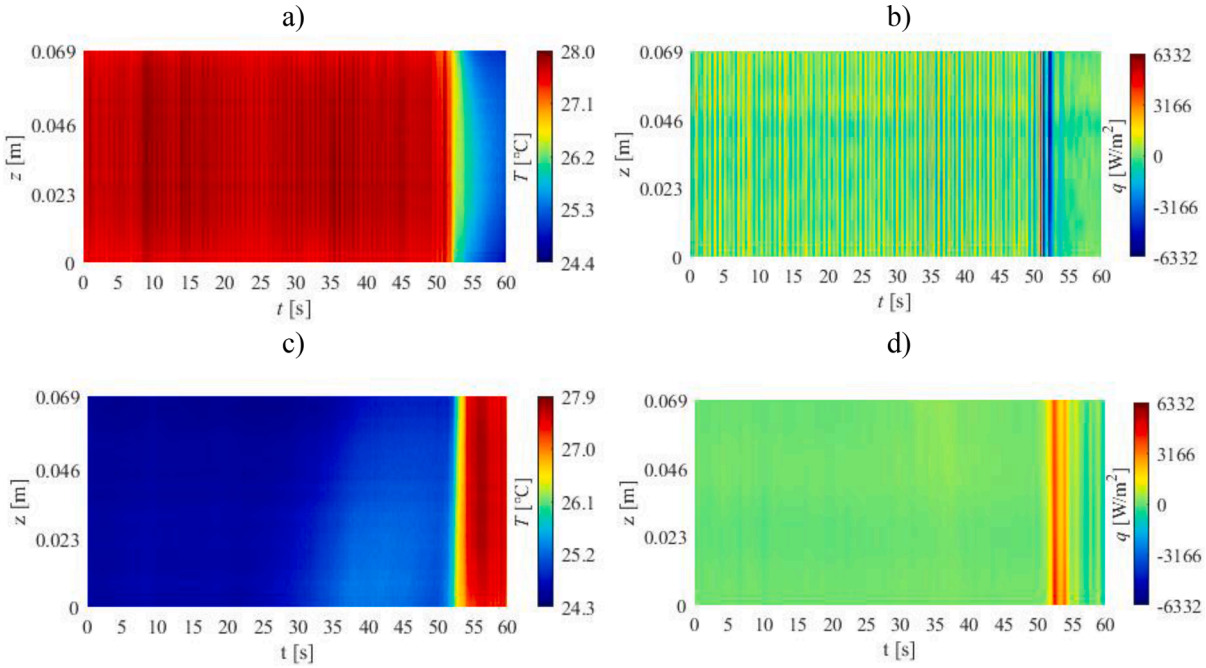

Fig. 9. Wall temperature distributions referred to channel 3 (a) and 4 (c), and corresponding wall-to-fluid heat flux distributions (b and d, respectively) during the oscillatory flow.

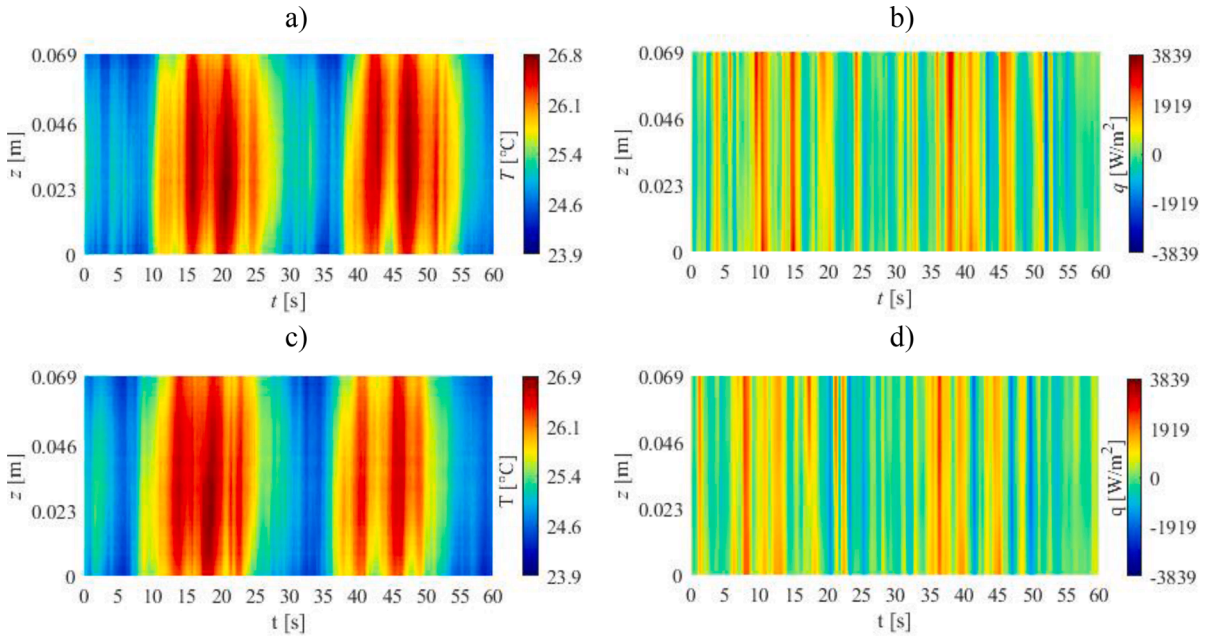

Fig. 10. Wall temperature distributions referred to channel 3 (a) and 4 (c), and corresponding wall-to-fluid heat flux distributions (b and d, respectively) during the circulatory flow.

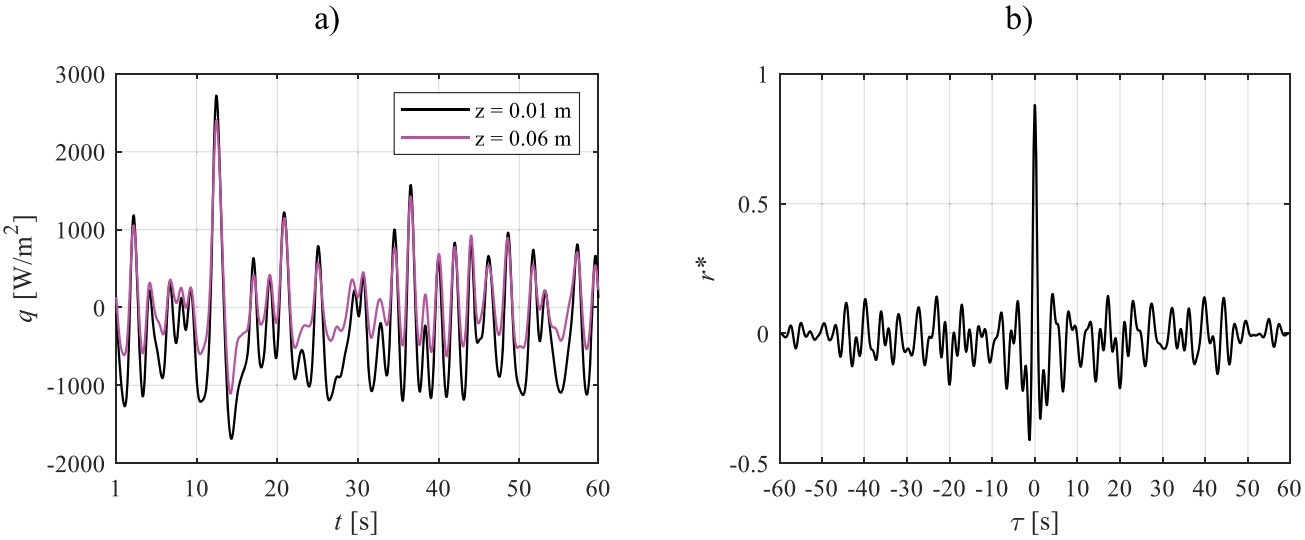

Fig. 11. HTDM applied to two spatial points belonging to the same PHP channel (number 11) at $Q = 70$ W, $T_{cond} = 10$ °C; iput heat fluxes (a) and resulting normalized cross-correlation (b).

observed flow direction is greatly expected during intermittent regimes, where the accumulated energy at the evaporator results in an impulsive fluid motion from the heated to the cooled sections.

Such an analysis on intermittent flows suggests that the thermal properties of the aluminium wall also play an important role in the fluid velocity evaluation. In fact, while persistent fluid oscillations tend to uniform the wall temperature and thermofluidic interactions over the channel length, impulsive fluid motions result in sudden increases of both quantities, sequentially along the tube. The latter experimental case partially reflects the one analysed in Section 3.3, where an impulsive thermofluidic phenomenon allowed the estimation of significant time delays at different fluid velocities.

4.3. Heat transfer delay method: application to the circulatory flow

As proven in [20] and in Section 4.1, during the circulatory flow, adjacent branches exhibit similar local wall-to-fluid heat flux distributions, shifted by a certain time delay. Such a behaviour is linked to the less chaotic and unidirectional motion of the working fluid, which is sequentially interested by similar cooling and heating phenomena in the condenser and the evaporator, respectively. The difficulties encountered in Section 4.2 can be therefore overcome by considering heat flux distributions referred to two spatial points in adjacent channels, i.e., at a longer distance. In Fig. 13, the heat fluxes referred to the same axial coordinate $z = 0.035$ m over time in channels 5 and 6 are shown along with the normalized cross-correlation between them, for $Q = 120$ W and $T_{cond} = 20$ °C.

Here, the cross-correlation (Fig. 13c) exhibits a significant peak at $\tau = 1.61$ s, denoting a distinguishable time delay between the two heat fluxes. Additionally, the positive τ suggests that the fluid first circulates in channel 6, and then in channel 5, confirming the fluid direction observed in [20]. The identification procedure for the time delay was

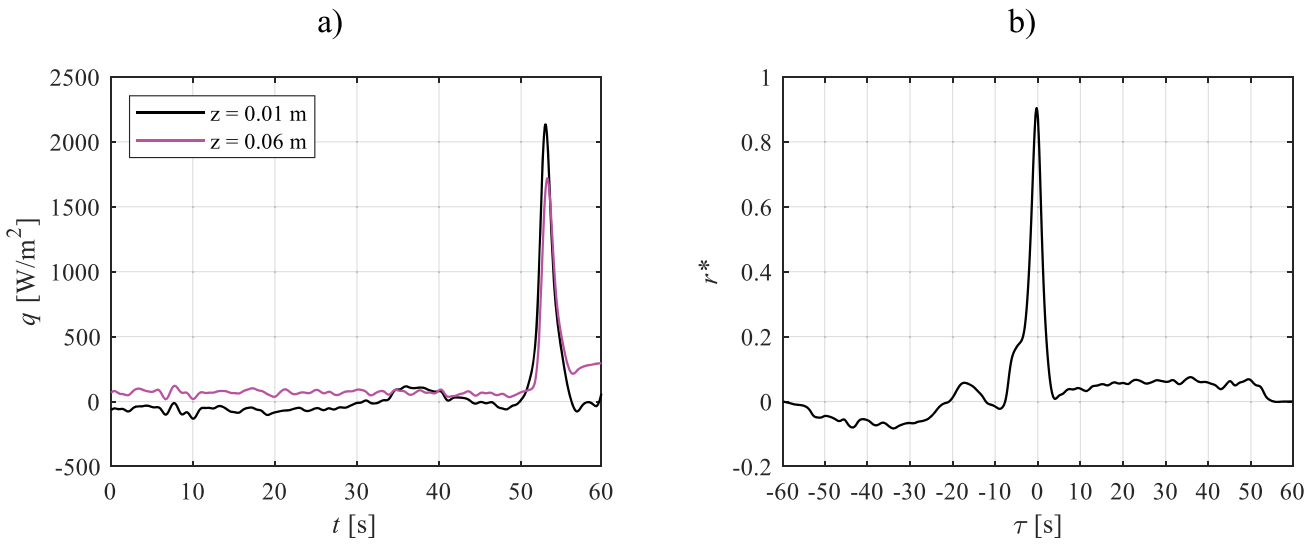

Fig. 12. HTDM applied to two spatial points belonging to the same channel; input heat fluxes (a) and resulting normalized cross-correlation (b).

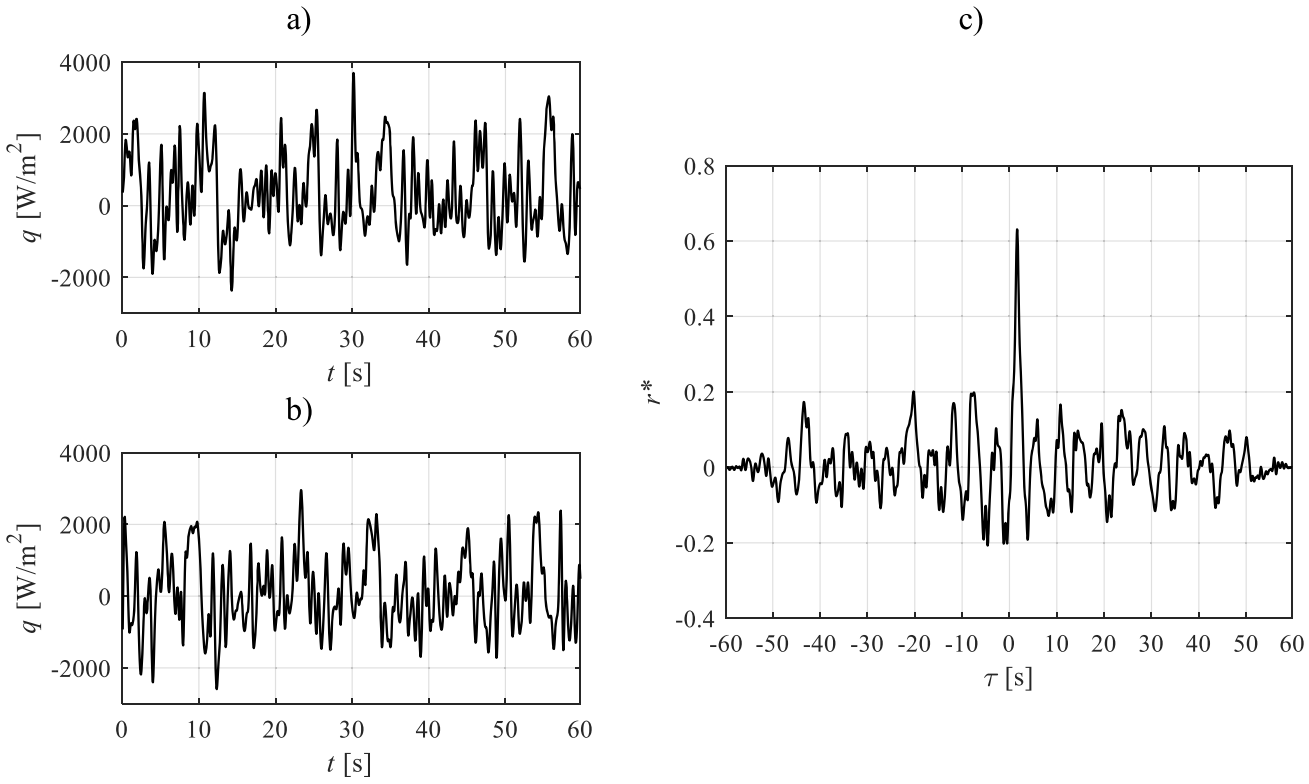

Fig. 13. Heat flux distributions for $Q = 120$ W, $T_{cond} = 20$ °C, channel 5 (a) and channel 6 (b), and normalized cross-correlation between them (c); both heat fluxes are referred to the fixed axial coordinate $z = 0.035$ m.

replicated by considering a pair of adjacent channels at a time, starting from channels 1 and 2. The resulting time delays τ are reported in Tables 5 and 6, for each channel pair, according to the channels' numeration of Fig. 1b.

It has to be noticed that, at high heat loads (from 150 W up to 210 W), the time delay provided by the present procedure could not be evaluated for every channel pair. This is due to the inner fluid dynamics of the studied PHP, which may consistently vary from low to high power inputs to the evaporator. Considering the formation of a stable slug-plug flow, the Bond criterion, which is a static criterion, is satisfied for the present application, but dynamic effects on the working fluid need to be considered, such as the inertial effects, which might significantly increase with the power input given to the evaporator. Such inertial effects can be evaluated by means of the Weber number (*We*), defined as [8]:

$$We = \frac{\rho_l U_l^2 d_{in}}{\sigma_l} \tag{9}$$

where ρ_l is the density of the liquid phase, U_l is the liquid slug velocity, d_{in} is the inner diameter and σ_l is the liquid surface tension. Analogously to the Bond criterion, the capillarity of the system is here usually verified when $We < 4$ [33]. For the present study case, the working fluid properties were evaluated by averaging the fluid temperature measured near

Table 5
Time delays referred to each channel pair; Tcond = 20 °C.

τ [s]	Q [W]				
Paired channels	90	120	150	180	190
1–2	1.98	1.61	0.71	0.63	1.11
2–3	1.85	1.49	0.84	0.48	0.23
3–4	1.89	1.57	0.88	–	–
4–5	1.93	1.54	0.44	0.48	–
5–6	1.99	1.63	0.8	1.31	1.11
6–7	2.10	1.63	1.57	1.24	–
7–8	1.90	1.56	1.56	1.17	0.56
8–9	2.19	1.60	1.78	0.47	–
9–10	1.84	1.53	1.54	0.54	1.12
10–11	1.83	1.42	–	–	1.22
11–12	1.78	1.34	–	–	–
12–13	1.67	1.44	–	–	–

Table 6
Time delays referred to each channel pair; Tcond = 10 °C.

τ [s]	Q [W]				
Paired channels	120	150	180	190	210
1–2	2.13	1.80	1.79	2.03	1.57
2–3	2.28	2.03	1.71	1.06	1.27
3–4	2.00	1.80	1.75	0.92	1.56
4–5	1.92	1.98	1.94	1.94	0.80
5–6	2.27	1.88	1.79	1.22	2.09
6–7	2.13	1.88	1.94	1.78	1.59
7–8	2.57	1.88	1.78	1.10	1.53
8–9	2.13	1.93	1.67	1.44	1.61
9–10	2.01	1.85	1.79	1.67	1.71
10–11	1.87	1.73	1.56	1.56	1.44
11–12	1.85	1.49	–	–	–
12–13	1.95	1.50	–	–	–

Table 7
Evaluated fluid velocities referred to each channel pair; Tcond = 20 °C.

v [m/s]	Q [W]				
Paired channels	90	120	150	180	190
1–2	0.22	0.27	0.61	0.69	0.39
2–3	0.24	0.29	0.52	0.91	1.89
3–4	0.23	0.28	0.49	–	–
4–5	0.23	0.28	0.99	0.91	–
5–6	0.22	0.27	0.54	0.33	0.39
6–7	0.21	0.27	0.28	0.35	–
7–8	0.23	0.28	0.28	0.37	0.78
8–9	0.19	0.27	0.24	0.93	–
9–10	0.24	0.28	0.28	0.81	0.39
10–11	0.24	0.31	–	–	0.36
11–12	0.24	0.32	–	–	–
12–13	0.26	0.30	–	–	–

Table 8
Evaluated fluid velocities referred to each channel pair; Tcond = 10 °C.

v [m/s]	Q [W]				
Paired channels	120	150	180	190	210
1–2	0.20	0.24	0.24	0.21	0.28
2–3	0.19	0.21	0.25	0.41	0.34
3–4	0.22	0.24	0.25	0.47	0.28
4–5	0.23	0.22	0.22	0.22	0.54
5–6	0.19	0.23	0.24	0.36	0.21
6–7	0.20	0.23	0.22	0.24	0.27
7–8	0.17	0.23	0.24	0.40	0.28
8–9	0.20	0.23	0.26	0.30	0.27
9–10	0.22	0.24	0.24	0.26	0.25
10–11	0.23	0.25	0.28	0.28	0.30
11–12	0.24	0.29	–	–	–
12–13	0.22	0.29	–	–	–

the evaporator and the condenser at 150 W, obtaining $T_{fluid} \approx 30$ °C. In addition, U_l was considered equal to 1 m/s since it is a representative value for fluid velocity in PHPs [8]. The resulting Weber number was found to be higher than 4, thus highlighting the possibility for the device to undergo transitions from slug-plug to dispersed flow, resulting in highly chaotic wall-to-fluid thermal interactions which undermine the evaluation of significant cross-correlations between wall-to-fluid heat fluxes locally exchanged in adjacent channels.

When extended to the present study case, Eq. (6) can be adopted for the evaluation of the fluid velocity between the two generic i th and $i+1$-th adjacent channels, thus assuming the following form:

$$v_{[i\rightarrow i+1]} = \frac{L_{[i\rightarrow i+1]}}{\tau_{[i\rightarrow i+1]}} \tag{10}$$

where $L_{[i \rightarrow i+1]}$ is the distance between the two spatial points at which q_i and q_{i+1} are assessed, i.e., the distance travelled by the working fluid, and $\tau_{[i \rightarrow i+1]}$ is the delay between the two considered heat flux signals. In particular, the travelled length $L_{[i \rightarrow i+1]}$ was considered, according to the geometry of the studied device, equal to 0.435± 0.001 m for every channel pair.

The fluid velocities, estimated by processing the data shown in Tables 5 and 6 through Eq. (10), are reported in Tables 7 and 8, respectively.

From the uncertainty analysis of Section 3.2, the uncertainty of the estimated fluid velocity, $\delta v_{[i \rightarrow i+1]}$, was found to range from about 3% for the longest perceived delay (2.19 s) up to a maximum of about 20% for the shortest perceived delay (0.23 s). The data reported in Tables 7 and 8 were furtherly reduced by computing their standard deviation for each heat load to the evaporator to evaluate differences over the whole device in terms of fluid velocity during circulation. The standard deviation of fluid velocity v_{std} is plotted in Fig. 14 for the two considered condenser temperatures.

For $T_{cond} = 20$ °C, v_{std} increases to 0.61 m/s, denoting that the circulatory flow is strongly independent of the considered channel pair at higher power inputs (≥ 150 W). This remark is in accordance with [16], where the maximum velocity referred to every channel tended to spread over a wider range at elevated heat loads. On the contrary, v_{std} assumes a more stable trend at $T_{cond} = 10$ °C, suggesting that a rise in fluid viscosity results in stronger dampening effects, i.e., higher uniformity of fluid velocity in the overall device.

By averaging $v_{[i \rightarrow i+1]}$ for the total number of channels n, i.e., for $i =$

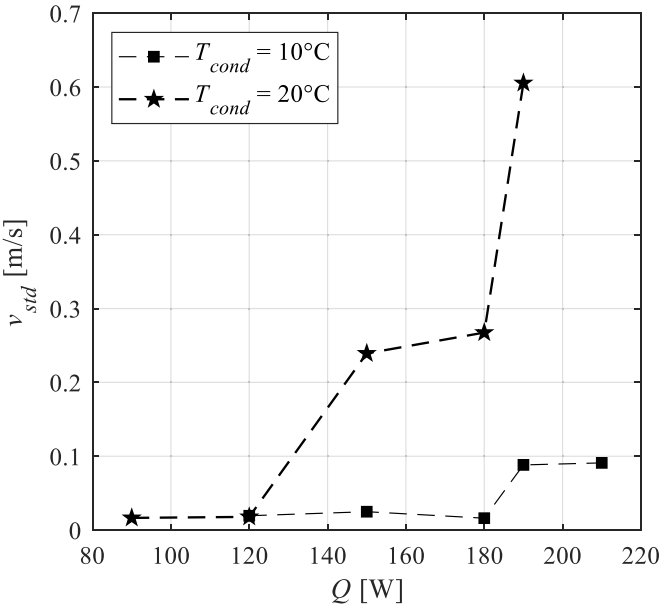

Fig. 14. Standard deviation of fluid velocity in the circulatory flow as a function of Q for the two analysed condenser temperatures.

1…*n*-1, at each heat load to the evaporator, the average fluid velocity during circulation in the overall device v_{av} was then evaluated and shown as a function of Q in Fig. 15. The uncertainty bands are also included; specifically, by considering the uncertainty referred to each velocity in Tables 7 and 8, the uncertainty of the average velocity δv_{av} is defined as [34]:

$$\delta v_{av} = \frac{\sqrt{\sum_{i=1}^{n-1}\left(\delta v_{[i\to i+1]}\right)^2}}{n-1} \tag{11}$$

where n is the total number of analysed channels. As already underlined in Section 3.3, since the uncertainty referred to higher velocities is higher than that at lower velocities, δv_{av} increases at higher heat loads, exhibiting here a maximum of ± 0.08 m/s at 190 W, T_{cond} = 20 °C.

For T_{cond} = 20 °C, the average velocity significantly increases with the power input given to the evaporator, ranging from a minimum of 0.23 m/s at Q = 90 W to a maximum on average equal to about 0.77 m/s at high heat loads. The estimated values of velocity are in great accordance with previous studies concerning high-speed visualizations [8,10,14,16], suggesting that the present approach provides quantitative pieces of data without increasing the complexity of the experimental set-up by adding transparent inserts to the PHP layout. On the contrary, the average fluid velocity undergoes a slight increase for T_{cond} = 10 °C, where v_{av} settles around 0.3 m/s at high heat loads. This is probably due to the fact that, by decreasing the condenser temperature and consequently the fluid temperature in the overall device, the viscosity of the working fluid increases [20], thus strongly hampering the fluid motion. Here, higher fluid viscosity might behave alike microgravity conditions tested in [17] and [15]. In fact, when the PHP operates in weightlessness, the fluid motion is strongly dampened by absence of buoyancy forces. When a qualitatively comparison is taken into account, high-viscosity and microgravity similarly affect the fluid stream, generally resulting in lower velocities which are less dependant on the heat load to the evaporator. Finally, the average fluid velocity was reduced with the aim of finding a correlation between v_{av} and Q. In particular, the average velocity data were fitted through a least-square approach by adapting the already existing model suggested by Patel and Mehta [16]. In other words, the optimal fitting of the data was expected to follow a power law of the form $y = bx^m$. In Fig. 16, the assessed correlation is shown for T_{cond} = 20 °C.

Some considerations can be drawn: first, the different b and m coefficients here estimated are reasonably due to the different properties of methanol, together with differences in terms of experimental set-up (geometry, boundary conditions at the heating sections, etc.…). Second, the estimated R^2 is slightly lower than the one provided in [16]; such a poorer correlating behaviour may be accounted for either a lower number of data points or different thermofluidic behaviour of the device. In fact, at 90 W and 190 W, the velocity trend appears to differ from the one perceived in the range 120–180 W, suggesting the presence of lower-power and higher-power velocity transition regions. The average velocities reported in [16] seem to confirm such transitions, although all the given data have been fitted by the authors through the same interpolating curve. Nonetheless, the given curve satisfactorily fits the data, suggesting that the power-law-based correlation may be extended to investigation cases other than those studied in [16]. Quantitative guidelines for the prediction of the correlation coefficients at various working conditions should be provided in future works, together with a full validation of the model. On the other hand, the employed power law was not able to correlate the data referred to T_{cond} = 10 °C, probably due to the complex interplay between buoyancy forces and viscous effects which undermine a straightforward comparison between low-viscosity and high-viscosity behaviours. A deeper velocity analysis on the viscosity-dominated operation is thus required.

5. Conclusions

A multi-turn pulsating heat pipe made of aluminium was tested in vertical bottom heated mode at different heat loads to the evaporator and condenser temperatures with the aim of evaluating the average fluid velocity by means of infrared thermography. The thermographic acquisitions were post-processed through the inverse heat conduction resolution approach, thus evaluating the wall-to-fluid heat flux exchanged within the adiabatic section. The heat flux distributions were therefore processed by means of an original technique based on the evaluation of normalized cross-correlation functions between adjacent channels, named Heat Transfer Delay Method. Such a method was experimentally validated by means of a dedicated loop, where hot water was forced to circulate at different velocities, ranging from 0.2 m/s up to 1 m/s. Here, the fluid velocity could be evaluated thanks to the non-intrusive, thermographic observation of temperature variations at the outer wall surface of the aluminium tube. The method was first applied

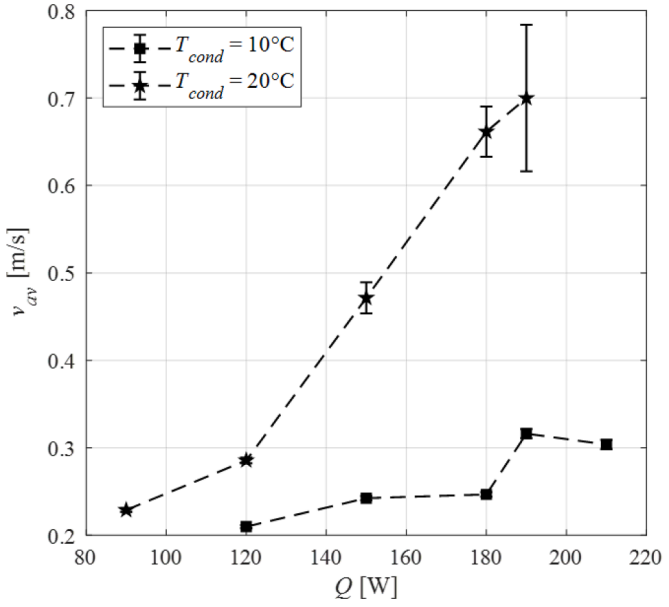

Fig. 15. Average fluid velocity in the circulatory flow as a function of Q for the two analysed condenser temperatures, along with uncertainty bars.

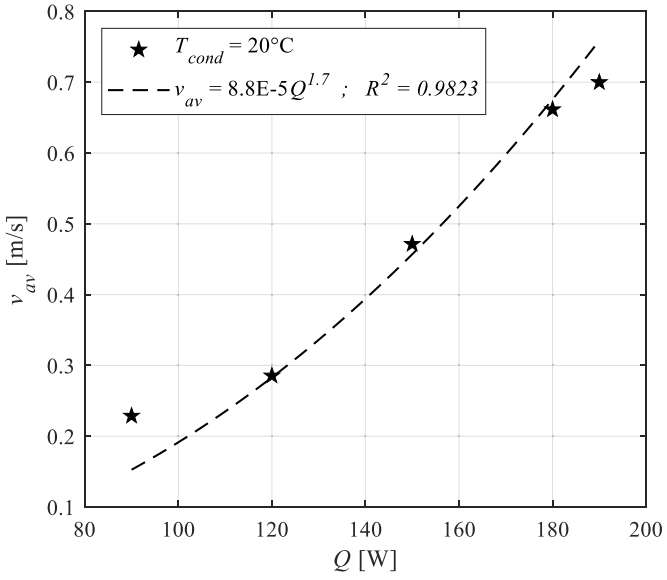

Fig. 16. Correlation between average fluid velocity during the circulatory flow and heat load to the evaporator; T_{cond} = 20 °C.

to the oscillatory flow mode, by considering two spatial points belonging to the same device channel. The circulatory flow mode was therefore studied by considering two spatial points belonging to two adjacent channels.

The main outcomes of the present experimental work are listed below:

- When the oscillatory flow is considered, null time delays prevent the evaluation of the fluid velocity, except for highly impulsive flow motions during the intermittent flow regime. This is probably due to the limited device dimensions and the thermal properties of the wall, coupled with high velocity of the working fluid. On the other hand, in the circulatory flow, similarities between adjacent channels in terms of local heat transfer behaviour allow the identification of significant time delays, i.e., of the fluid velocity, at farther points.
- For fluid velocities lower than 0.2 m/s (longer time delays), the estimation error for the HTDM is equal to 3%, while, for velocities greater than 1 m/s (shorter time delays), it is higher than 20%.
- The fluid velocities substantially vary from channel pair to channel pair, especially at high condenser temperature and higher heat loads to the evaporator.
- At $T_{cond} = 20$ °C, the average fluid velocity v_{av} during the circulatory flow monotonically increases from 0.23 m/s up to a maximum of about 0.7 m/s at 90 W and 190 W, respectively. At $T_{cond} = 10$ °C, the average fluid velocity settles instead around 0.3 m/s for almost every considered heat load, probably due to the more predominant viscous effects.
- For $T_{cond} = 20$ °C, the average fluid velocity can be satisfactorily expressed as a function of the heat load by means of the relationship $v_{av} = 8.8\text{E-}5Q^{1.7}$. Such a power law, which has been extrapolated for comparison from [16], may be thus employed in the prediction of fluid velocities in Pulsating Heat Pipes. Further analyses are however needed to provide a full validation of the model, as well as quantitative guidelines for the identification of the correlation coefficients at different working conditions. Future studies are also required to establish a modified correlation for the viscosity-dominated operation.

To conclude, the presented approach represents an interesting method for the fluid velocity evaluation on such devices where no high-speed visualizations of fluid pressure measurements can be performed. The Heat Transfer Delay Method can be extended to the study of other PHPs, as long as the thermal properties of their walls guarantee perceivable temperature variations at the outer wall surface. Moreover, the study of longer PHPs may promote the fluid velocity evaluation during the oscillatory flow.

Declaration of Competing Interest

The authors declare that they have no known competing financial interests or personal relationships that could have appeared to influence the work reported in this paper.

Data availability

The data that has been used is confidential.

Acknowledgments

The work has been carried out through a fruitful and effective collaboration between the University of Parma and the University of Pisa. The Authors would like to acknowledge the European Space Agency (ESA) support through the grant 4000128640/19/NL/PG/pt, ESA MAP project TOPDESS.

References

[1] S.M. Sohel Murshed, C.A. Nieto de Castro, A critical review of traditional and emerging techniques and fluids for electronics cooling, Renew. Sustain. Energy Rev. 78 (2017) 821–833, https://doi.org/10.1016/J.RSER.2017.04.112.
[2] M. Moustaid, V. Platel, M. Guillet, H. Reynes, C. Buttay, Modeling and test of a thermosyphon loop for the cooling of a megawatt-range power electronics converter, Int. J. Thermofluids 13 (2022), 100129, https://doi.org/10.1016/j.ijft.2021.100129.
[3] A.J. Robinson, J. Colenbrander, T. Deaville, J. Durfee, R. Kempers, A wicked heat pipe fabricated using metal additive manufacturing, Int. J. Thermofluids 12 (2021), 100117, https://doi.org/10.1016/j.ijft.2021.100117.
[4] R.R. Riehl, S.M.S. Murshed, Performance evaluation of nanofluids in loop heat pipes and oscillating heat pipes, Int. J. Thermofluids 14 (2022), 100147, https://doi.org/10.1016/j.ijft.2022.100147.
[5] D. Bastakoti, H. Zhang, D. Li, W. Cai, F. Li, An overview on the developing trend of pulsating heat pipe and its performance, Appl. Therm. Eng. 141 (2018) 305–332, https://doi.org/10.1016/J.APPLTHERMALENG.2018.05.121.
[6] Y. Xu, Y. Xue, H. Qi, W. Cai, An updated review on working fluids, operation mechanisms, and applications of pulsating heat pipes, Renew. Sustain. Energy Rev. 144 (2021) 110995, https://doi.org/10.1016/j.rser.2021.110995.
[7] M. Mameli, G. Besagni, P.K. Bansal, C.N. Markides, Innovations in pulsating heat pipes: from origins to future perspectives, Appl. Therm. Eng. 203 (2022), 117921, https://doi.org/10.1016/j.applthermaleng.2021.117921.
[8] M. Marengo, V.S. Nikolayev. Pulsating heat pipes: experimental analysis, design and applications, 2018, pp. 1–62, https://doi.org/10.1142/9789813234406_0001.
[9] M. Mameli, M. Marengo, S. Khandekar, Local heat transfer measurement and thermo-fluid characterization of a pulsating heat pipe, Int. J. Therm. Sci. 75 (2014) 140–152, https://doi.org/10.1016/j.ijthermalsci.2013.07.025.
[10] Z.H. Xue, W. Qu, Experimental and theoretical research on a ammonia pulsating heat pipe: new full visualization of flow pattern and operating mechanism study, Int. J. Heat Mass Transf. 106 (2017) 149–166, https://doi.org/10.1016/j.ijheatmasstransfer.2016.09.042.
[11] G. Spinato, N. Borhani, J.R. Thome, Understanding the self-sustained oscillating two-phase flow motion in a closed loop pulsating heat pipe, Energy 90 (2015) 889–899, https://doi.org/10.1016/j.energy.2015.07.119.
[12] S. Lips, A. Bensalem, Y. Bertin, V. Ayel, C. Romestant, J. Bonjour, Experimental evidences of distinct heat transfer regimes in pulsating heat pipes (PHP), Appl. Therm. Eng. 30 (2010) 900–907, https://doi.org/10.1016/j.applthermaleng.2009.12.020.
[13] B.Y. Tong, T.N. Wong, K.T. Ooi, Closed-loop pulsating heat pipe, Appl. Therm. Eng. 21 (2001) 1845–1862, https://doi.org/10.1016/S1359-4311(01)00063-1.
[14] J.L. Xu, Y.X. Li, T.N. Wong, High speed flow visualization of a closed loop pulsating heat pipe, Int. J. Heat Mass Transf. 48 (2005) 3338–3351, https://doi.org/10.1016/j.ijheatmasstransfer.2005.02.034.
[15] L. Pietrasanta, M. Mameli, D. Mangini, A. Georgoulas, N. Michè, S. Filippeschi, M. Marengo, Developing flow pattern maps for accelerated two-phase capillary flows, Exp. Therm. Fluid Sci. 112 (2020), 109981, https://doi.org/10.1016/j.expthermflusci.2019.109981.
[16] V.M. Patel, H.B. Mehta, Channel wise displacement-velocity-frequency analysis in acetone charged multi-turn closed loop pulsating heat pipe, Energy Convers. Manag. 195 (2019) 367–383, https://doi.org/10.1016/j.enconman.2019.05.014.
[17] R. Perna, M. Abela, M. Mameli, A. Mariotti, L. Pietrasanta, M. Marengo, S. Filippeschi, Flow characterization of a pulsating heat pipe through the wavelet analysis of pressure signals, Appl. Therm. Eng. 171 (2020), 115128, https://doi.org/10.1016/j.applthermaleng.2020.115128.
[18] D. Mangini, M. Mameli, A. Georgoulas, L. Araneo, S. Filippeschi, M. Marengo, A pulsating heat pipe for space applications: ground and microgravity experiments, Int. J. Therm. Sci. 95 (2015) 53–63, https://doi.org/10.1016/j.ijthermalsci.2015.04.001.
[19] M. Abela, M. Mameli, V. Nikolayev, S. Filippeschi, Experimental analysis and transient numerical simulation of a large diameter pulsating heat pipe in microgravity conditions, Int. J. Heat Mass Transf. 187 (2022), 122532, https://doi.org/10.1016/j.ijheatmasstransfer.2022.122532.
[20] L. Pagliarini, L. Cattani, M. Mameli, S. Filippeschi, F. Bozzoli, S. Rainieri, Global and local heat transfer behaviour of a three-dimensional Pulsating Heat Pipe: combined effect of the heat load, orientation and condenser temperature, Appl. Therm. Eng. 195 (2021), 117144, https://doi.org/10.1016/j.applthermaleng.2021.117144.
[21] N. Iwata, F. Bozzoli, L. Pagliarini, L. Cattani, P. Vocale, M. Malavasi, S. Rainieri, Characterization of thermal behavior of a micro pulsating heat pipe by local heat transfer investigation, Int. J. Heat Mass Transf. 196 (2022), 123203, https://doi.org/10.1016/j.ijheatmasstransfer.2022.123203.
[22] L. Pagliarini, L. Cattani, F. Bozzoli, M. Mameli, S. Filippeschi, S. Rainieri, M. Marengo, Thermal characterization of a multi-turn pulsating heat pipe in microgravity conditions: statistical approach to the local wall-to-fluid heat flux, Int. J. Heat Mass Transf. 169 (2021), 120930, https://doi.org/10.1016/j.ijheatmasstransfer.2021.120930.
[23] M. Mameli, A. Catarsi, D. Mangini, L. Pietrasanta, N. Michè, M. Marengo, P. di Marco, S. Filippeschi, Start-up in microgravity and local thermodynamic states of a hybrid loop thermosyphon/pulsating heat pipe, Appl. Therm. Eng. 158 (2019), 113771, https://doi.org/10.1016/j.applthermaleng.2019.113771.
[24] G. Maranzana, S. Didierjean, B. Rémy, D. Maillet, Experimental estimation of the transient free convection heat transfer coefficient on a vertical flat plate in air, Int. J. Heat Mass Transf. 45 (2002) 3413–3427, https://doi.org/10.1016/S0017-9310(02)00049-2.

[25] J. v Beck, B. Blackwell, C.R.S. Clair Jr, Inverse Heat Conduction: Ill-Posed Problems, James Beck, 1985.
[26] D.A. Murio, The mollification method and the numerical solution of ill-posed problems, John Wiley \& Sons (1993).
[27] D. Delpueyo, X. Balandraud, M. Grédiac, Heat source reconstruction from noisy temperature fields using an optimised derivative Gaussian filter, Infrared Phys. Technol. 60 (2013) 312–322, https://doi.org/10.1016/J.INFRARED.2013.06.004.
[28] F. Bozzoli, G. Pagliarini, S. Rainieri, Experimental validation of the filtering technique approach applied to the restoration of the heat source field, Exp. Therm. Fluid Sci. 44 (2013) 858–867, https://doi.org/10.1016/j.expthermflusci.2012.10.002.
[29] V.A. Morozov, Methods For Solving Incorrectly Posed Problems, Springer-Verlag, 1984.
[30] P. Stoica, R.L. Moses. Spectral Analysis of Signals, Pearson/Prentice Hall, Upper Saddle River, N.J., 2008, https://doi.org/10.1109/msp.2007.273066.
[31] S.J. Kline, Describing uncertainties in single-sample experiments, Mech. Eng. 75 (1953) 3–8.
[32] Bakker, P., van Vliet, L.J., Verbeek, P.W., Edge preserving orientation adaptive filtering, Proceedings of the 1999 IEEE computer society conference on computer vision and pattern recognition (Cat. No PR00149), 1999: 535–540.1. 10.1109/CVPR.1999.786989.
[33] J. Gu, M. Kawaji, R. Futamata, Effects of gravity on the performance of pulsating heat pipes, J. Thermophys. Heat Trans. 18 (2004) 370–378, https://doi.org/10.2514/1.3067.
[34] J. Taylor, Introduction to error analysis, the study of uncertainties in physical measurements, 1997.